Accepted Manuscript

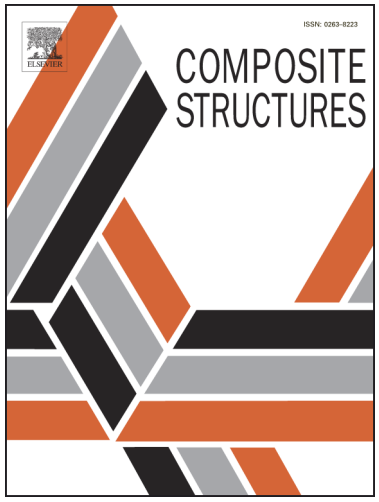

Dynamic instability of functionally graded multilayer graphene nanocomposite beams in thermal environment

Helong Wu, Jie Yang, Sritawat Kitipornchai

PII: S0263-8223(16)32499-0
DOI: http://dx.doi.org/10.1016/j.compstruct.2016.12.001
Reference: COST 8056

To appear in: *Composite Structures*

Received Date: 10 November 2016
Revised Date: 29 November 2016
Accepted Date: 2 December 2016

Please cite this article as: Wu, H., Yang, J., Kitipornchai, S., Dynamic instability of functionally graded multilayer graphene nanocomposite beams in thermal environment, *Composite Structures* (2016), doi: http://dx.doi.org/10.1016/j.compstruct.2016.12.001

Dynamic instability of functionally graded multilayer graphene nano-composite beams in thermal environment

Helong Wu[1], Jie Yang[2,*], Sritawat Kitipornchai[1]

[1] School of Civil Engineering, The University of Queensland, Brisbane, St Lucia 4072, Australia

[2] School of Engineering, RMIT University, PO Box 71, Bundoora, VIC 3083 Australia

Dynamic instability of functionally graded multilayer graphene nanocomposite beams in thermal environment

Helong Wu[1], Jie Yang[2,*], Sritawat Kitipornchai[1]

[1] School of Civil Engineering, The University of Queensland, Brisbane, St Lucia 4072, Australia

[2] School of Engineering, RMIT University, PO Box 71, Bundoora, VIC 3083 Australia

---

Abstract

This paper studies the dynamic instability of functionally graded multilayer nanocomposite beams reinforced with a low content of graphene nanoplatelets (GPLs) and subjected to a combined action of a periodic axial force and a temperature change. The weight fraction of GPL nanofillers is assumed to be constant in each individual GPL-reinforced composite (GPLRC) layer but follows a layerwise variation across the beam thickness. The Halpin-Tsai micromechanics model is used to estimate the effective Young's modulus of GPLRC layers. The differential quadrature method is employed to convert the partial differential governing equations into a linear system of Mathieu-Hill equations, from which the principle unstable region of functionally graded multilayer GPLRC beams is determined by Bolotin's method. Special attention is given to the effects of GPL distribution pattern, weight fraction, geometry and dimension on the dynamic instability behaviour. The thermal buckling and free vibration are also discussed as subset problems. Numerical results show that distributing more GPLs near the top and bottom surfaces can effectively increase the natural frequency and reduce the size of the unstable region. The influences of GPL geometry and dimension tend to be insignificant when the GPL width-to-thickness ratio is larger than 10^3.

Keywords: graphene nanoplatelets; functionally graded nanocomposites; dynamic instability; thermal buckling; free vibration.

1. Introduction

Polymer nanocomposites in which nanofillers such as carbon nanotubes (CNTs), graphene and its derivatives are dispersed in a polymer matrix have been attracting considerable attention from both research and engineering communities [1]. Compared with the conventional polymer composites, polymer nanocomposites exhibit significantly higher stiffness and strength due to the superiorly high moduli of nanofillers, together with the nanoscale effects and interface chemistry [2-4].

---

* Corresponding author. Tel.: 61-03-99256169; Fax: 61-03-99256108

E-mail address: j.yang@rmit.edu.au (J. Yang)

Since the first observations in the early 1990s [5, 6], CNTs are considered promising reinforcement materials for high performance structural composites due to their exceptionally mechanical, thermal and electrical properties [7-9]. In order to make better use of a low content of CNTs, Shen [10] applied the functionally graded concept to polymer nanocomposites and found that the mechanical properties can be further improved through a nonuniform distribution of CNTs in the polymer matrix. Subsequently, the mechanical responses of functionally graded CNT-reinforced composite (FG-CNTRC) structures have been extensively investigated [11-14]. Among those, Ke et al. [15] examined the dynamic stability behaviour of FG-CNTRC beams under a periodic axial force. Yang et al. [16] studied the dynamic buckling of thermo-electro-mechanically loaded FG-CNTRC beams integrated with piezoelectric layers. Lei et al. [17] presented a dynamic stability analysis of FG-CNTRC cylindrical panels. These studies [15-17] revealed that the distribution pattern and volume fraction of CNTs have important influences on the dynamic stability behaviour of polymer nanocomposite structures. Although significant advances have been made in CNTs filled nanocomposites, agglomeration and relatively high production cost have hindered the further applications of CNTs as reinforcement materials in polymer nanocomposites [18].

Graphene [19] is a two-dimensional monolayer of carbon atoms with remarkable physical properties and chemical functionalisation capabilities [20-22]. Compared to CNTs, graphene has comparable tensile strength (130 GPa) and Young's modulus (~1 TPa) [20] but a much larger surface area of up to 2630 $m^2 g^{-1}$ [23]. More importantly, graphene and its derivatives are abundant in nature and less expensive when synthesized in large scale [24]. These merits make graphene and its derivatives excellent alternatives to CNTs while improving the mechanical properties of polymeric materials. The superiority of graphene as a promising reinforcement material was further verified by recent studies [25] that demonstrated that the graphene nanocomposites exhibit significantly higher Young's modulus and tensile strength than the nanocomposites reinforced with the same amount of CNTs.

Rafiee et al. [25] measured and compared the mechanical properties of epoxy nanocomposites reinforced with 0.1wt% of graphene nanoplatelets (GPLs) and CNTs, respectively. They found that the Young's modulus, tensile strength and fracture toughness of graphene nanocomposites are significantly higher than those of pristine epoxy and that GPLs dramatically outperform CNTs in terms of mechanical properties enhancement. Wang et al. [26] experimentally investigated the thermal properties of graphene nanocomposites. Their test results indicated that incorporation of graphene oxide sheets reduces the thermal expansion coefficients and considerably increases the thermal conductivity of the polymer matrix. By using Mori-Tanaka micromechanics method, Ji et al. [4] examined the stiffening effect of graphene sheets dispersed in polymer nanocomposites. Their results showed that the addition of a very low content of graphene sheets can remarkably increase the effective stiffness of the nanocomposite. Zhao et al. [27] reported that a loading of 1.8vol% graphene results in a 150% improvement in tensile strength and a nearly 10 times increase in Young's modulus of poly (vinyl alcohol) nanocomposites. Liu et al. [28] successfully fabricated GPL-reinforced alumina ceramic composites using Spark Plasma Sintering and observed that the resulting flexural strength and fracture toughness are significantly higher than those of monolithic ceramic

samples. Rahman and Haque [29] studied the effects of GPL concentration, aspect ratio and dispersion on elastic constants and stress-strain responses of graphene/epoxy nanocomposites using molecular mechanics and molecular dynamics simulations. Liu et al. [30] used a stacking and folding method to generate aligned graphene/polycarbonate composites that considerably enhances effective elastic modulus and strength of the primitive polycarbonate even at an exceptionally low loading of graphene.

Owing to the mechanical advantages of high strength and stiffness but low density, graphene nanocomposites show tremendous potentials for development of advanced lightweight engineering structures in the forms of beam, plate, as well as shell structural elements that are vital in aeronautical and space industries. However, all the aforementioned studies on graphene nanocomposites were focused on the synthesis and material property characterization only. Investigations on the mechanical behaviour of engineering structures made of such advanced nanocomposites are very limited. Most recently, Rafiee et al. [31] experimentally studied the buckling of graphene/epoxy nanocomposite beam structures. Significant increase (up to 52%) in critical buckling load was observed by adding only 0.1 wt% of GPLs into the epoxy matrix. Song et al. [32] carried out the free and forced vibration analysis of functionally graded multilayer GPL/polymer nanocomposite plates and suggested that the incorporation of a small amount of GPLs can significantly increase the natural frequencies and reduce the dynamic deflection of plates under pulse loading. As far as the authors are aware, no previous work has been done on the dynamic instability of graphene nanocomposite structures.

Hence, this paper is devoted to the investigation of the dynamic instability of functionally graded multilayer graphene nanoplatelet-reinforced composite (GPLRC) beams under a periodic axial force and a temperature change. A multilayer beam model with a layer-wise variation in GPL concentration is used since an ideal functionally graded nanocomposite structure with a continuous and smooth change in GPL content across the beam thickness is extremely difficult to fabricate due to the limitation of current manufacture technology. Obviously, such a multilayer structure with an adequate number of layers is an excellent approximation of the ideal functionally graded structure. It is assumed that each individual layer is made from a mixture of uniformly dispersed GPL nanofillers and polymer matrix and its effective Young's modulus is predicted by Halpin-Tsai micromechanics model. Governing equations are derived based on the first-order shear deformation beam theory (FSDT) and converted into a linear system of Mathieu-Hill equations by using differential quadrature method, after which the principle unstable region is obtained by using Bolotin's method. Parametric studies are conducted to examine the effects of GPL distribution pattern, weight fraction, geometry and dimension, the static axial force, as well as the temperature change on the dynamic instability behaviour of functionally graded multilayer GPLRC beams. Thermal buckling and free vibration are also discussed as subset problems.

2. Effective material properties of GPLRCs

Fig. 1(a) shows a multilayer beam composed of perfectly bonded GPLRC layers of same thickness h_L. It is assumed that the GPLRC layer is made from a mixture of an isotropic

polymer matrix and rectangular shaped GPLs that are randomly oriented and uniformly dispersed. Hence, each individual GPLRC layer is isotropic homogeneous and its effective Young's modulus can be estimated by Halpin-Tsai micromechanics model [33-35]

$$E=\frac{3}{8}\frac{1+\xi_{\mathrm{L}}\eta_{\mathrm{L}}V_{\mathrm{GPL}}}{1-\eta_{\mathrm{L}}V_{\mathrm{GPL}}}\times E_{\mathrm{m}}+\frac{5}{8}\frac{1+\xi_{\mathrm{T}}\eta_{\mathrm{T}}V_{\mathrm{GPL}}}{1-\eta_{\mathrm{T}}V_{\mathrm{GPL}}}\times E_{\mathrm{m}}, \tag{1}$$

where parameters η_{L} and η_{T} take the following forms:

$$\eta_{\mathrm{L}}=\frac{\left(E_{\mathrm{GPL}}/E_{\mathrm{m}}\right)-1}{\left(E_{\mathrm{GPL}}/E_{\mathrm{m}}\right)+\xi_{\mathrm{L}}},\ \eta_{\mathrm{T}}=\frac{\left(E_{\mathrm{GPL}}/E_{\mathrm{m}}\right)-1}{\left(E_{\mathrm{GPL}}/E_{\mathrm{m}}\right)+\xi_{\mathrm{T}}}. \tag{2}$$

where E_{GPL} and E_{m} are Young's moduli of the GPL and matrix, respectively. V_{GPL} is the volume fraction of GPL nanofillers. Note that Eq. (1) does take into account GPL's geometry and dimension through geometry factors ξ_{L} and ξ_{T} which are defined by [33]

$$\xi_{\mathrm{L}}=2\left(a_{\mathrm{GPL}}/t_{\mathrm{GPL}}\right),\ \xi_{\mathrm{T}}=2\left(b_{\mathrm{GPL}}/t_{\mathrm{GPL}}\right), \tag{3}$$

where a_{GPL}, b_{GPL} and t_{GPL} are the length, width and thickness of GPLs, respectively. Here, ξ_{L} can be rewritten as

$$\xi_{\mathrm{L}}=2\left(a_{\mathrm{GPL}}/b_{\mathrm{GPL}}\right)\times\left(b_{\mathrm{GPL}}/t_{\mathrm{GPL}}\right), \tag{4}$$

in which $a_{\mathrm{GPL}}/b_{\mathrm{GPL}}$ *a*nd $b_{\mathrm{GPL}}/t_{\mathrm{GPL}}$ are GPL aspect ratio and width-to-thickness ratio, respectively.

According to the rule of mixture, the effective linear thermal expansion coefficient α, mass density ρ, and Poisson's ratio ν of the GPLRC are expressed as

$$\alpha=\alpha_{\mathrm{m}}V_{\mathrm{m}}+\alpha_{\mathrm{GPL}}V_{\mathrm{GPL}}, \tag{5}$$

$$\rho=\rho_{\mathrm{m}}V_{\mathrm{m}}+\rho_{\mathrm{GPL}}V_{\mathrm{GPL}}, \tag{6}$$

$$\nu=\nu_{\mathrm{m}}V_{\mathrm{m}}+\nu_{\mathrm{GPL}}V_{\mathrm{GPL}}, \tag{7}$$

where α_{GPL} and α_{m} are thermal expansion coefficients, with the subscript "GPL" and "m" referring to the GPLs and matrix, respectively. ρ_{GPL} and ρ_{m} are mass densities; ν_{GPL} and ν_{m} are Poisson's ratios; the volume fractions V_{GPL} and V_{m} are related by $V_{\mathrm{m}}+V_{\mathrm{GPL}}=1$.

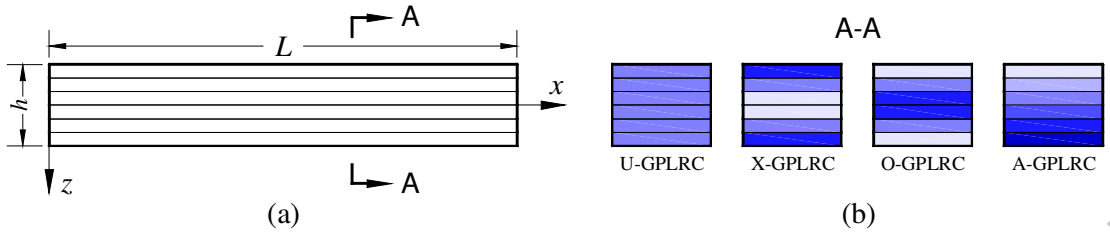

Fig. 1 Configuration and coordinate system of a multilayer GPLRC beam.

Shown in Fig. 1(b) are the uniform (U) and functionally graded (X, O and A) distributions of GPL nanofillers in the thickness direction of the beam in which the darker colour represents a higher content of GPLs within the layer. Since the GPL content remains constant across all layers in the uniform distribution, U-GPLRC corresponds to an isotropic homogeneous beam. In the functionally graded distributions, however, GPL weight fraction varies from layer to layer in such a way that both the top and bottom layers are GPL rich in an X-GPLRC beam while this is inversed in an O-GPLRC beam where the middle layers are GPL rich. The GPL content gradually increases from the top layer to the bottom layer in an A-GPLRC beam.

Without the loss of generality, it is assumed that the multilayer GPLRC beam consists of an even number of layers. The GPL volume fraction of the k^{th} layer for the four GPL distribution patterns depicted in Fig. 1(b) are given as

$$\text{U-GPLRC: } V_{\text{GPL}}^{(k)} = V_{\text{GPL}}^{*}, \tag{8}$$

$$\text{X-GPLRC: } V_{\text{GPL}}^{(k)} = 2V_{\text{GPL}}^{*}\left|2k - N_{\text{L}} - 1\right|/N_{\text{L}}, \tag{9}$$

$$\text{O-GPLRC: } V_{\text{GPL}}^{(k)} = 2V_{\text{GPL}}^{*}\left(1 - \left|2k - N_{\text{L}} - 1\right|/N_{\text{L}}\right), \tag{10}$$

$$\text{A-GPLRC: } V_{\text{GPL}}^{(k)} = V_{\text{GPL}}^{*}\left(2k - 1\right)/N_{\text{L}}, \tag{11}$$

in which N_{L} is the total number of layers of the beam and $k = 1, 2, \ldots, N_{\text{L}}$. V_{GPL}^{*} is the total GPL volume fraction that is determined by

$$V_{\text{GPL}}^{*} = \frac{W_{\text{GPL}}}{W_{\text{GPL}} + \left(\rho_{\text{GPL}}/\rho_{\text{m}}\right)\left(1 - W_{\text{GPL}}\right)}, \tag{12}$$

where W_{GPL} is the total GPL weight fraction in the whole beam. As is evident from Eqs. (8)-(11), the total volume fractions of GPLs in the U-, X-, O- and A-GPLRC beams are the same.

3. Theoretical formulations

3.1 Governing equations

Consider a multilayer GPLRC beam of length L, total thickness h, and subjected to a combined action of an axial dynamic force N_{x0} and a uniform temperature change $\Delta T = T - T_0$ from the initial stress-free state at the reference temperature T_0. Based on the FSDT, the displacements of an arbitrary point parallel to the -x and -z axes are given as

$$\overline{U}(x,z,t) = U(x,t) + z\psi(x,t),\ \overline{W}(x,\ z,t) = W(x,t), \tag{13}$$

where U and W are the longitudinal and transverse displacement components in the mid-plane ($z = 0$); ψ is the rotation angle of the normal to the mid-plane and t is time. The linear strain-displacement relations give

$$\varepsilon_{xx} = \frac{\partial U}{\partial x} + z\frac{\partial \psi}{\partial x},\ \gamma_{xz} = \frac{\partial W}{\partial x} + \psi. \tag{14}$$

The linear stress-strain relations take the form

$$\sigma_{xx} = Q_{11}\left(\frac{\partial U}{\partial x} + z\frac{\partial \psi}{\partial x} - \alpha\Delta T\right),\ \sigma_{xz} = Q_{55}\left(\frac{\partial W}{\partial x} + \psi\right), \tag{15}$$

in which the plane stress-reduced stiffness Q_{11} and Q_{55} are

$$Q_{11} = \frac{E}{1-\nu^2},\ Q_{55} = \frac{E}{2(1+\nu)}. \tag{16}$$

The governing equations of the beam can be derived using the principle of virtual displacements:

$$0 = \int_{t_1}^{t_2}\left(\delta\Upsilon_{\mathrm{p}} + \delta K - \delta V\right)\mathrm{d}t, \tag{17}$$

where the virtual work $\delta\Upsilon_{\mathrm{p}}$ done by external loads, virtual kinetic energy δK, and the virtual strain energy δV are given by

$$\delta\Upsilon_{\mathrm{p}} = \int_0^L\left(N_{x0} + N_x^T\right)\frac{\partial W}{\partial x}\frac{\partial \delta W}{\partial x}\mathrm{d}x, \tag{18}$$

$$\delta K = \int_0^L\int_{-h/2}^{h/2}\rho\left[\left(\frac{\partial U}{\partial t} + z\frac{\partial \psi}{\partial t}\right)\left(\frac{\partial \delta U}{\partial t} + z\frac{\partial \delta\psi}{\partial t}\right) + \frac{\partial W}{\partial t}\frac{\partial \delta W}{\partial t}\right]\mathrm{d}z\mathrm{d}x, \tag{19}$$

$$\delta V = \int_0^L\int_{-h/2}^{h/2}\left[\sigma_{xx}\left(\frac{\partial \delta U}{\partial x} + z\frac{\partial \delta\psi}{\partial x}\right) + \sigma_{xy}\left(\frac{\partial \delta W}{\partial x} + \delta\psi\right)\right]\mathrm{d}z\mathrm{d}x. \tag{20}$$

in which N_x^T is the thermally induced axial force due to a uniform temperature rise. Substituting for $\delta\Upsilon_{\mathrm{p}}$, δK, and δV from Eqs. (18)-(20) into virtual work statement in Eq. (17) and integrating through the beam thickness, we obtain

$$\begin{aligned}0=\int_{t_1}^{t_2}\int_0^L\Bigg[&\left(\frac{\partial N_x}{\partial x}-I_0\frac{\partial^2 U}{\partial t^2}-I_1\frac{\partial^2\psi}{\partial t^2}\right)\delta U+\left(\frac{\partial Q_x}{\partial x}-N_{x0}\frac{\partial^2 W}{\partial x^2}-N_x^T\frac{\partial^2 W}{\partial x^2}-I_0\frac{\partial^2 W}{\partial t^2}\right)\delta W\\&+\left(\frac{\partial M_x}{\partial x}-Q_x-I_1\frac{\partial^2 U}{\partial t^2}-I_2\frac{\partial^2\psi}{\partial t^2}\right)\delta\psi\Bigg]\mathrm{d}x\mathrm{d}t\\&-\int_{t_1}^{t_2}\left[\left(N_x\delta U\right)\Big|_0^L+\left(M_x\delta\psi\right)\Big|_0^L-\left(Q_x-N_{x0}\frac{\partial W}{\partial x}-N_x^T\frac{\partial W}{\partial x}\right)\delta W\Big|_0^L\right]\mathrm{d}t\end{aligned},\tag{21}$$

where the in-plane force and moment resultants are calculated from

$$N_x=A_{11}\frac{\partial U}{\partial x}+B_{11}\frac{\partial\psi}{\partial x}-N_x^T,\tag{22}$$

$$M_x=B_{11}\frac{\partial U}{\partial x}+D_{11}\frac{\partial\psi}{\partial x}-M_x^T,\tag{23}$$

$$Q_x=\kappa A_{55}\left(\frac{\partial W}{\partial x}+\psi\right),\tag{24}$$

in which $\kappa=5/6$ is the shear correction factor. The k^{th} GPLRC layer is located between the points $z=z_k$ and $z=z_{k+1}$ in the thickness direction. The stiffness components and inertia related terms are defined as

$$\left\{A_{11},B_{11},D_{11}\right\}=\int_{-h/2}^{h/2}Q_{11}\{1,z,z^2\}\mathrm{d}z=\sum_{k=1}^{N_L}\int_{z_k}^{z_{k+1}}Q_{11}^{(k)}\{1,z,z^2\}\mathrm{d}z,\tag{25}$$

$$A_{55}=\int_{-h/2}^{h/2}Q_{55}\mathrm{d}z=\sum_{k=1}^{N_L}\int_{z_k}^{z_{k+1}}Q_{55}^{(k)}\mathrm{d}z.\tag{26}$$

$$\left\{I_0,I_1,I_2\right\}=\int_{-h/2}^{h/2}\rho\{1,z,z^2\}\mathrm{d}z=\sum_{k=1}^{N_L}\int_{z_k}^{z_{k+1}}\rho^{(k)}\{1,z,z^2\}\mathrm{d}z.\tag{27}$$

The thermally induced force and moment are given by

$$\left\{N_x^{\mathrm{T}},M_x^{\mathrm{T}}\right\}=\int_{-h/2}^{h/2}Q_{11}\alpha\Delta T\left\{1,z\right\}\mathrm{d}z=\sum_{k=1}^{N_L}\int_{z_k}^{z_{k+1}}Q_{11}^{(k)}\alpha^{(k)}\Delta T\left\{1,z\right\}\mathrm{d}z.\tag{28}$$

In the above equations, $Q_{11}^{(k)}$, $Q_{55}^{(k)}$, $\rho^{(k)}$, and $\alpha^{(k)}$ are the values of Q_{11}, Q_{55}, ρ, and α of the k^{th} GPLRC layer, respectively.

Keeping Eqs. (22)-(24) in mind and setting the coefficients of δU, δW, and $\delta\psi$ in Eq. (21) to zero separately, the governing equations can be obtained in terms of displacements as

$$A_{11}\frac{\partial^2 U}{\partial x^2}+B_{11}\frac{\partial^2 \psi}{\partial x^2}=I_0\frac{\partial^2 U}{\partial t^2}+I_1\frac{\partial^2 \psi}{\partial t^2}, \tag{29}$$

$$\kappa A_{55}\left(\frac{\partial^2 W}{\partial x^2}+\frac{\partial \psi}{\partial x}\right)-\left(N_{x0}+N_x^{\mathrm{T}}\right)\frac{\partial^2 W}{\partial x^2}=I_0\frac{\partial^2 W}{\partial t^2}, \tag{30}$$

$$B_{11}\frac{\partial^2 U}{\partial x^2}+D_{11}\frac{\partial^2 \psi}{\partial x^2}-\kappa A_{55}\left(\frac{\partial W}{\partial x}+\psi\right)=I_1\frac{\partial^2 U}{\partial t^2}+I_2\frac{\partial^2 \psi}{\partial t^2}. \tag{31}$$

Note that for a uniform temperature variation the derivatives of thermal force N_x^{T} and moment M_x^{T} with respect to x are zero and consequently are omitted in the governing equations. In the present analysis, multilayer GPLRC beams either clamped or hinged at the ends (i.e. $x = 0, L$) are considered. The associated boundary conditions are:

Clamped (C): $U = 0$, $W = 0$, $\psi = 0$, (32)

Hinged (H): $U = 0$, $W = 0$, $B_{11}\dfrac{\partial U}{\partial x}+D_{11}\dfrac{\partial \psi}{\partial x}-M_x^{T}=0$. (33)

By introducing the following dimensionless quantities:

$$\begin{aligned}
&\zeta = x/L,\ \lambda = L/h,\ \{u, w\}=\{U, W\}/h,\ \varphi=\psi,\ \left\{P, P^{\mathrm{T}}, M^{\mathrm{T}}\right\}=\left\{N_{x0}, N_x^{\mathrm{T}}, M_x^{\mathrm{T}}/h\right\}/A_{110},\\
&\left\{a_{11}, a_{55}, b_{11}, d_{11}\right\}=\left\{A_{11}, \kappa A_{55}, B_{11}/h, D_{11}/h^2\right\}/A_{110},\ \left\{I_{\mathrm{a}}, I_{\mathrm{b}}, I_{\mathrm{c}}\right\}=\left\{I_0, I_1/h, I_2/h^2\right\}/I_{00},\\
&\tau = t\sqrt{A_{110}/I_{00}}/L,\ (\omega,\theta)=(\Omega,\Theta)L\sqrt{I_{00}/A_{110}},
\end{aligned} \tag{34}$$

where A_{110} and I_{00} are the values of A_{11} and I_0 of a homogeneous beam made from the pure matrix material, ω and θ are the dimensionless forms of the natural frequency Ω and excitation frequency Θ, the governing equations (29)-(31) and associated boundary conditions (32) and (33) can be rewritten in dimensionless form as

$$a_{11}\frac{\partial^2 u}{\partial \zeta^2}+b_{11}\frac{\partial^2 \varphi}{\partial \zeta^2}=I_{\mathrm{a}}\frac{\partial^2 u}{\partial \tau^2}+I_{\mathrm{b}}\frac{\partial^2 \varphi}{\partial \tau^2}, \tag{35}$$

$$a_{55}\left(\frac{\partial^2 w}{\partial \zeta^2}+\lambda\frac{\partial \varphi}{\partial \zeta}\right)-\left(P+P^{\mathrm{T}}\right)\frac{\partial^2 w}{\partial \zeta^2}=I_{\mathrm{a}}\frac{\partial^2 w}{\partial \tau^2}, \tag{36}$$

$$b_{11}\frac{\partial^2 u}{\partial \zeta^2}+d_{11}\frac{\partial^2 \varphi}{\partial \zeta^2}-\lambda a_{55}\left(\frac{\partial w}{\partial \zeta}+\lambda\varphi\right)=I_{\mathrm{b}}\frac{\partial^2 u}{\partial \tau^2}+I_{\mathrm{c}}\frac{\partial^2 \varphi}{\partial \tau^2}; \tag{37}$$

Clamped (C): $u = 0$, $w = 0$, $\varphi = 0$, (38)

Hinged (H): $u = 0$, $w = 0$, $b_{11}\dfrac{\partial u}{\partial \zeta} + d_{11}\dfrac{\partial \varphi}{\partial \zeta} - M^{\mathrm{T}} = 0$. (39)

3.2 Solution method

The differential quadrature approach combined with Bolotin's method is employed to study the dynamic instability characteristics of functionally graded multilayer GPLRC beams. The basic idea is to convert the partial differential governing equations into a set of linear algebraic equations through the differential quadrature approximation in the ζ-axis, from which the principle unstable region is then determined by using Bolotin's method.

According to the differential quadrature rule [36-38], the unknown displacement components u, w, φ and their j^{th} partial derivatives with respect to ζ are approximated by

$$\{u, w, \varphi\} = \sum_{m=1}^{N} l_m(\zeta)\{u_m, w_m, \varphi_m\}, \text{ and } \frac{\partial^j}{\partial \zeta^j}\{u, w, \varphi\}\bigg|_{\zeta=\zeta_i} = \sum_{m=1}^{N} C_{im}^{(j)}\{u_m, w_m, \varphi_m\}, \tag{40}$$

where $\{u_m, w_m, \varphi_m\}$ are the values of $\{u, w, \varphi\}$ at $\zeta = \zeta_m$; $l_m(\zeta)$ is the Lagrange interpolation polynomials; $C_{im}^{(j)}$ is the weighting coefficient for the j^{th} partial derivative of unknown displacement components with respect to ζ and its recursive formula can be found in [39, 40]. N is the total number of grid points that are located along the ζ-axis according to a cosine pattern as

$$\zeta_i = \frac{1}{2}\left[1 - \cos\frac{\pi(i-1)}{N-1}\right],\ i = 1, 2, \ldots, N. \tag{41}$$

Applying the relationship (40) to the dimensionless partial differential governing equations (35)-(37) yields

$$a_{11}\sum_{m=1}^{N} C_{im}^{(2)} u_m + b_{11}\sum_{m=1}^{N} C_{im}^{(2)} \varphi_m = I_{\mathrm{a}}\ddot{u}_i + I_{\mathrm{b}}\ddot{\varphi}_i, \tag{42}$$

$$a_{55}\left(\sum_{m=1}^{N} C_{im}^{(2)} w_m + \lambda\sum_{m=1}^{N} C_{im}^{(1)} \varphi_m\right) - \left(P + P^{\mathrm{T}}\right)\times\sum_{m=1}^{N} C_{im}^{(2)} w_m = I_{\mathrm{a}}\ddot{w}_i, \tag{43}$$

$$b_{11}\sum_{m=1}^{N} C_{im}^{(2)} u_m + d_{11}\sum_{m=1}^{N} C_{im}^{(2)} \varphi_m - \lambda a_{55}\left(\sum_{m=1}^{N} C_{im}^{(1)} w_m + \lambda\varphi_i\right) = I_{\mathrm{b}}\ddot{u}_i + I_{\mathrm{c}}\ddot{\varphi}_i. \tag{44}$$

The dimensionless boundary conditions in Eqs. (38) and (39) can be handled in the same way as

$$u_1 = 0,\ w_1 = 0,\ \varphi_1 = 0, \tag{45}$$

$$u_N = 0,\ w_N = 0,\ \varphi_N = 0, \tag{46}$$

for the beam with clamped ends at $\zeta = 0$ and 1, respectively, and

$$u_1 = 0,\ w_1 = 0,\ b_{11}\sum_{m=1}^{N} C_{1m}^{(1)} u_m + d_{11}\sum_{m=1}^{N} C_{1m}^{(1)} \varphi_m - \lambda M^{\mathrm{T}}\big|_{\zeta=\zeta_1} = 0, \tag{47}$$

$$u_N = 0,\ w_N = 0,\ b_{11}\sum_{m=1}^{N} C_{Nm}^{(1)} u_m + d_{11}\sum_{m=1}^{N} C_{Nm}^{(1)} \varphi_m - \lambda M^{\mathrm{T}}\big|_{\zeta=\zeta_N} = 0, \tag{48}$$

for the beam with hinged ends at $\zeta = 0$, 1.

In view of Eq. (28) and keeping Eq. (34) in mind, substitution of the associated boundary conditions into the governing equations (42)-(44) leads to a set of dimensionless linear algebraic equations that can be expressed in matrix form as

$$\mathbf{M}\ddot{\mathbf{d}} + \left(\mathbf{K}_{\mathrm{L}} - \Delta T\mathbf{K}_{\mathrm{T}} - P\mathbf{K}_{\mathrm{P}}\right)\mathbf{d} = \mathbf{0}, \tag{49}$$

in which the over dot denotes the partial derivative with respect to dimensionless time τ; $\mathbf{M}$ and $\mathbf{K}_{\mathrm{L}}$ are the mass matrix and stiffness matrix, respectively; $\mathbf{K}_{\mathrm{T}}$ and $\mathbf{K}_{\mathrm{P}}$ are the geometric stiffness matrices. It is obvious that these matrices are directly dependent on material property gradient and beam geometry. The unknown displacement vector $\mathbf{d}$ is composed of u_i, w_i, φ_i as follows:

$$\mathbf{d} = \left\{\{u_i\}^{\mathrm{T}}, \{w_i\}^{\mathrm{T}}, \{\varphi_i\}^{\mathrm{T}}\right\}^{\mathrm{T}},\ i = 1, 2, \ldots, N. \tag{50}$$

For the beam under a time-varying axial excitation, the dimensionless axial force P is expressed as

$$P = P_{\mathrm{s}} + P_{\mathrm{d}}\cos\theta\tau, \tag{51}$$

where P_{s} and P_{d} are the static and dynamic force components, respectively. By substituting for P from Eq. (51), Eq. (49) can be rewritten as

$$\mathbf{M}\ddot{\mathbf{d}} + \left[\mathbf{K}_{\mathrm{L}} - \Delta T\mathbf{K}_{\mathrm{T}} - \left(P_{\mathrm{s}} + P_{\mathrm{d}}\cos\theta\tau\right)\mathbf{K}_{\mathrm{P}}\right]\mathbf{d} = \mathbf{0}. \tag{52}$$

Eq. (52) is a Mathieu-Hill type equation describing the dynamic instability behaviour of functionally graded multilayer GPLRC beams subjected to a periodic axial force and a tempera-

ture change. The Bolotin's method [41] is used to determine the boundary of the unstable region. In this paper, we seek the solutions with a period $2T_\theta$ ($T_\theta = 2\pi/\theta$) only due to the fact that the region of instability situated near $\theta = 2\omega$, namely principal unstable region, is of the greatest practical importance. The periodic solution of Eq. (52) with a period $2T_\theta$ takes the form of a trigonometric series as

$$\mathbf{d} = \sum_{n=1,3,\ldots}^{\infty} \mathbf{a}_n \sin\frac{n\theta\tau}{2} + \mathbf{b}_n \cos\frac{n\theta\tau}{2}, \tag{53}$$

where $\mathbf{a}_n$ and $\mathbf{b}_n$ are arbitrary constant vectors. Bolotin [41] demonstrated that the first approximation with $n = 1$ can be used to calculate the boundary of the region of instability with a desired accuracy. In this case, substituting Eq. (53) into Eq. (52) and equating the coefficients of identical $\sin(\theta\tau/2)$ and $\cos(\theta\tau/2)$ leads to the following system of linear homogeneous algebraic equations in terms of $\mathbf{a}_1$ and $\mathbf{b}_1$:

$$\left[\mathbf{K}_\mathrm{L} - \Delta T\mathbf{K}_\mathrm{T} - \left(P_\mathrm{s} - \frac{P_\mathrm{d}}{2}\right)\mathbf{K}_\mathrm{p} - \frac{\theta^2}{4}\mathbf{M}\right]\mathbf{a}_1 = \mathbf{0}, \tag{54}$$

$$\left[\mathbf{K}_\mathrm{L} - \Delta T\mathbf{K}_\mathrm{T} - \left(P_\mathrm{s} + \frac{P_\mathrm{d}}{2}\right)\mathbf{K}_\mathrm{p} - \frac{\theta^2}{4}\mathbf{M}\right]\mathbf{b}_1 = \mathbf{0}, \tag{55}$$

from which two critical excitation frequencies θ at each given dynamic force P_d can be found as eigenvalues. The plot of θ against P_d gives two curves that show the principle unstable regions of functionally graded multilayer GPLRC beams. The intersection point at $P_\mathrm{d} = 0$ is the origin of principle unstable region and corresponds to the doubled fundamental frequency of the beam.

It is should be mentioned that Eq. (52) can also be used to analyse several subset problems, such as thermal buckling and free vibration of functionally graded multilayer GPLRC beams under thermo-mechanical loading. By neglecting the inertia terms and setting P_s and P_d to zero, the critical buckling temperature rise can be obtained by solving the following eigenvalue equation:

$$\left(\mathbf{K}_\mathrm{L} - \Delta T\mathbf{K}_\mathrm{T}\right)\mathbf{d} = \mathbf{0}. \tag{56}$$

For the free vibration problem, the dynamic load component $P_\mathrm{d} = 0$ and $\mathbf{d} = \mathbf{d}^* e^{i\omega\tau}$ is used to separate the spatial variable ζ and time τ. Then Eq. (52) is rewritten as

$$\left[\mathbf{K}_\mathrm{L} - \Delta T\mathbf{K}_\mathrm{T} - P_\mathrm{s}\mathbf{K}_\mathrm{p} - \omega^2\mathbf{M}\right]\mathbf{d}^* = \mathbf{0}, \tag{57}$$

from which the natural frequencies of the beam under a static axial force and a temperature change can be found through a standard eigenvalue algorithm.

4. Numerical examples and discussion

In this section, numerical results are presented to investigate the dynamic instability characteristics of functionally graded multilayer GPLRC beams that are subjected to a combined periodic axial force and a uniform temperature change. Thermal buckling and free vibration are also discussed as subset problems.

In what follows, the functionally graded multilayer GPLRC beams with a total thickness h = 0.01 m are considered. Each GPLRC layer is made from a mixture of the epoxy and GPLs with a length of a_{GPL} = 2.5 μm, width of b_{GPL} = 1.5 μm and thickness of t_{GPL} = 1.5 nm [25]. The material properties of both the epoxy and GPLs are assumed to be temperature-independent and are listed in Table 1.

Table 1 Material properties of the epoxy and GPLs.

Material properties	Epoxy [42]	GPL [25]
Young's modulus (GPa)	3.0	1010
Density (kg m^{-3})	1200	1062.5
Poisson's ratio	0.34	0.186 [43]
Thermal expansion coefficient (×10^{-6} /K)	60	5.0 [44]

4.1 Convergence and validation

Convergence study is first undertaken by comparing numerical solutions with varying numbers of grid points and layers in Table 2 where P_{cr} and ω_1 denote the dimensionless critical buckling load and fundamental frequency, respectively, and ΔT_{cr} is the critical buckling temperature rise. As observed, the present solutions converge very well when the total numbers of grid points and individual layers are increased to N = 11 and N_L = 40, respectively. Nonetheless, the tiny difference between the results with N_L = 10 and N_L = +∞ suggests that a multilayer GPLRC beam with 10 layers is sufficiently accurate to model an idea functionally graded beam with continuous variation in both material composition and properties. Taking into account the ease of fabrication and the manufacturing cost, N_L = 10, as well as N = 11, are used in all of the following numerical calculations.

Table 2 Buckling and free vibration results with varying total numbers of grid points and layers for a C-C functionally graded multilayer X-GPLRC beam (L/h = 30, W_{GPL} = 0.3%).

N (N_L = 10)	P_{cr}	ΔT_{cr} (K)	ω_1	N_L (N = 11)	P_{cr}	ΔT_{cr} (K)	ω_1
5	0.0108	90.335	0.3387	4	0.0085	71.448	0.3280
7	0.0089	74.622	0.3349	6	0.0088	73.505	0.3327
9	0.0089	74.561	0.3350	10	0.0089	74.557	0.3350
11	0.0089	74.557	0.3350	20	0.0089	75.001	0.3360
13	0.0089	74.557	0.3350	40	0.0090	75.112	0.3362
15	0.0089	74.557	0.3350	+∞	0.0090	75.149	0.3363

In order to validate the present analysis, direct comparisons between our results and those in the literature are made in Tables 3-5 and Fig. 2. The dimensionless critical buckling temperature rises for cross-ply (0/90/0) laminated composite beams are calculated and compared in Table 3 with those by Khdeir [45]. The elastic constants used in this instance are $G_{12} = G_{13} = 0.6E_{22}$, $G_{23} = 0.5E_{22}$, $\alpha_{22}/\alpha_{11} = 3$, and $\nu_{12} = 0.25$. As can be seen, the present results are almost identical to the existing ones.

The dimensionless critical buckling loads and natural frequencies of FGM beams are given in Tables 4 and 5, respectively, together with those of Ke et al. [46]. In addition, the principal unstable region of a clamped-sliding FGM beam is given and compared in Fig. 2 with that given by Yan et al. [47]. The material properties used in these examples follow an exponential law variation across the beam thickness with $E_1 = 70$ GPa, $\rho_1 = 2780$ kg m^{-3}, $\nu_1 = 0.33$. Again, our results agree very well with those reported in the literature.

Table 3 Comparison of dimensionless critical buckling temperature rises $\lambda_T = \Delta T_{cr}\alpha_1 (L/h)^2$ for cross-ply (0/90/0) laminated composite beams (L/h = 10).

E_{22}/E_{11}	C-C		C-H		H-H	
	Present	Ref. [45]	Present	Ref. [45]	Present	Ref. [45]
3	2.6558	2.6558	1.4691	1.4691	0.7625	0.7625
10	2.4725	2.4725	1.5367	1.5367	0.8868	0.8868
20	1.8858	1.8859	1.2896	1.2896	0.8281	0.8281

Table 4 Comparison of dimensionless critical buckling loads for C-C FGM beams.

E_2/E_1	L/h = 6		L/h = 16	
	Present	Ref. [46]	Present	Ref. [46]
0.2	0.03111	0.03111	0.00542	0.00542
1.0	0.06885	0.06884	0.01229	0.01227
5.0	0.15554	0.15554	0.02709	0.02709

Table 5 Comparison of the first three dimensionless natural frequencies for FGM beams (E_2/E_1 = 5.0, L/h = 16).

Source	C-C			H-H		
	ω_1	ω_2	ω_3	ω_1	ω_2	ω_3
Present	0.3693	0.9858	1.8573	0.1800	0.6510	1.4367
Ref. [46]	0.3686	0.9783	1.8287	0.1797	0.6482	1.4176

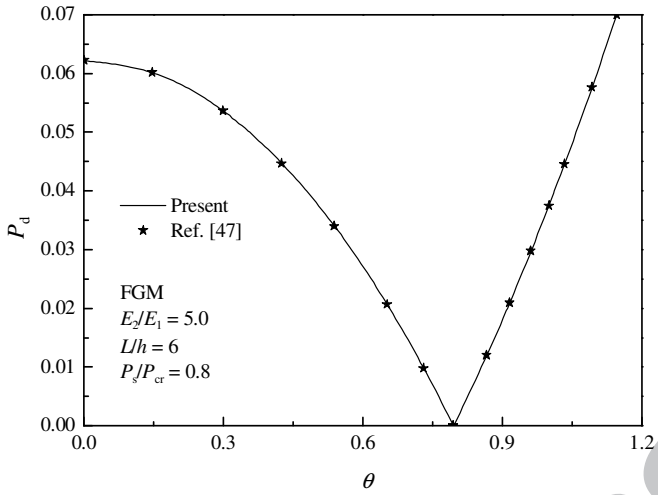

Fig. 2. Comparison of the principal unstable region for a clamped-sliding FGM beam.

4.2 Thermal buckling

The thermal buckling results of functionally graded multilayer GPLRC beams with various parameters are presented in Figs. 3 and 5 and Table 6.

Fig. 3 investigates the effects of GPL distribution pattern and weight fraction on the critical buckling temperature rise of C-C functionally graded multilayer GPLRC beams with a slenderness ratio $L/h = 30$. The results show that the critical buckling temperature of the X-GPLRC beam increases with an increase in GPL weight fraction, while this is not the case for A- and O-GPLRC beams whose critical buckling temperatures decrease as the GPL weight fraction grows, with the former being less noticeable than the latter. This effect becomes much less pronounced when GPL weight fraction exceeds a certain value. In contrast, the critical buckling temperature remains nearly unchanged for the U-GPLRC beam as GPL content increases. This can be explained by the relationship between the critical buckling load P_{cr} and critical buckling temperature rise ΔT_{cr}

$$P_{cr} = \Delta T_{cr}\int_{-h/2}^{h/2} Q_{11}\alpha \mathrm{d}z = \Delta T_{cr}\sum_{k=1}^{N_L}\int_{z_k}^{z_{k+1}} Q_{11}^{(k)}\alpha^{(k)}\mathrm{d}z = \Delta T_{cr}\left(h_L\sum_{k=1}^{N_L} Q_{11}^{(k)}\alpha^{(k)}\right) = \eta\Delta T_{cr}, \tag{58}$$

where h_L is the thickness of each GPLRC layer. The parameter η is dependent on the total GPL weight fraction only, implying that η has the same value for different GPL distribution patterns at the same GPL weight fraction. For the U-GPLRC beam, Eq. (58) is simplified as

$$P_{cr}^{U} = \Delta T_{cr}^{U}\left(Q_{11}\alpha h\right) = \eta\Delta T_{cr}^{U}, \tag{59}$$

and the bending stiffness can be expressed as

$$D_{11} = \int_{-h/2}^{h/2} Q_{11}z^2\mathrm{d}z = Q_{11}h^3/12. \tag{60}$$

Combining Eqs. (59) and (60), the critical buckling load P_{cr}^{U} of the U-GPLRC beam can be re-expressed as

$$P_{cr}^{U} = \Delta T_{cr}^{U}\left(Q_{11}\alpha h\right) = \Delta T_{cr}^{U}\left(12D_{11}\alpha/h^{2}\right) = \eta\Delta T_{cr}^{U}. \tag{61}$$

According to the FSDT, the critical buckling load increases almost linearly with the increase of bending stiffness [48], where the "almost" is used here due to the shear deformation effect. Reminding Eq. (61), it is clear that the critical buckling load is proportional to the bending stiffness, indicating that the ratio of P_{cr}^{U} to η, i.e. the critical buckling temperature rise ΔT_{cr}^{U}, is a constant for the U-GPLRC beam, regardless of the change of GPL weight fraction. In addition, based on the authors' recent work [49], the variation of critical buckling load with the GPL weight fraction is obtained and shown in Fig. 4. It is observed that the critical buckling loads of the beams with different GPL distribution patterns can be approximated as a linear function of GPL weight fraction as

$$\left\{P_{cr}^{X}, P_{cr}^{U}, P_{cr}^{A}, P_{cr}^{O}\right\} = \left\{k_{X}, k_{U}, k_{A}, k_{O}\right\}W_{GPL} + P_{cr}^{0}, \ (k_{X} > k_{U} > k_{A} > k_{O} > 0), \tag{62}$$

in which $P_{cr}^{X}, P_{cr}^{U}, P_{cr}^{A}, P_{cr}^{O}$ are critical buckling loads, $k_{X}, k_{U}, k_{A}, k_{O}$ are slopes, with the superscript/subscript X, U, A, and O referring to the distribution patterns X, U, A, and O, respectively. P_{cr}^{0} is the critical buckling load at W_{GPL} = 0.0% (i.e. the pure epoxy beam). The ratio of P_{cr}^{X} to η, i.e. the critical buckling temperature rise ΔT_{cr}^{X} of the X-GPLRC beam is given as

$$\Delta T_{cr}^{X} = P_{cr}^{X}/\eta = P_{cr}^{X}/P_{cr}^{U} \times P_{cr}^{U}/\eta = \Delta T_{cr}^{U}\left(k_{X}W_{GPL} + P_{cr}^{0}\right)/\left(k_{U}W_{GPL} + P_{cr}^{0}\right), \tag{63}$$

where ΔT_{cr}^{U}, as explained above, is a constant. It is clear from Eq. (63) that ΔT_{cr}^{X} increases as the GPL weight fraction W_{GPL} increases due to $k_{X} > k_{U}$. Moreover, ΔT_{cr}^{X} converges to a constant value of $\Delta T_{cr}^{U}k_{X}/k_{U}$ when W_{GPL} is sufficiently large. In the same way, one can understand why the critical buckling temperatures of A- and O-GPLRC beams are reduced with the GPL weight fraction growing and the effect of GPL weight fraction becomes much less pronounced at a higher value of W_{GPL}. The results in Fig. 3 clearly indicate that among the four distribution patterns, pattern X is capable of reinforcing the thermal buckling performance of the nanocomposite beams.

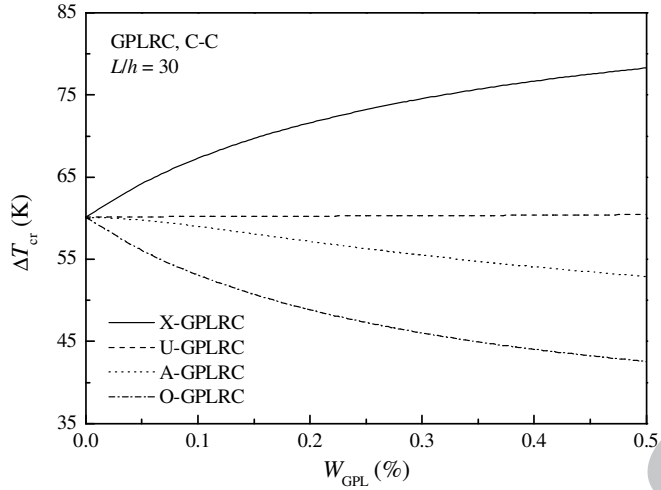

Fig. 3. Effects of GPL distribution pattern and weight fraction on the critical buckling temperature rise of functionally graded multilayer GPLRC beams.

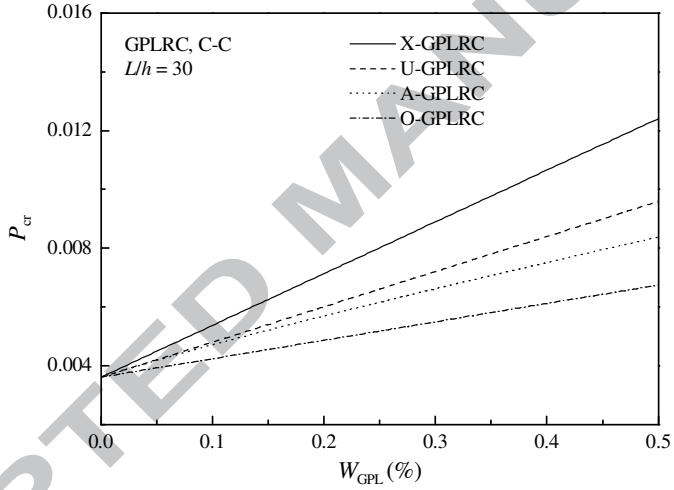

Fig. 4. Effects of GPL distribution pattern and weight fraction on the critical buckling load of functionally graded multilayer GPLRC beams.

Fig. 5 depicts the effects of GPL geometry and dimension, in the form of aspect ratio a_{GPL}/b_{GPL} and width-to-thickness ratio b_{GPL}/t_{GPL}, on the critical buckling temperature rise of C-C functionally graded multilayer GPLRC beams (W_{GPL} = 0.3%, L/h = 30) where GPL width b_{GPL} is kept constant. In such a case, a higher value of a_{GPL}/b_{GPL} represents a larger surface area, while a greater magnitude of b_{GPL}/t_{GPL} means that an individual GPL consists of fewer single graphene sheets. The critical buckling temperature of the X-GPLRC beam increases as both a_{GPL}/b_{GPL} and b_{GPL}/t_{GPL} increase. However, this is reversed for O- and A GPLRC beams, whose critical buckling temperature drops with an increase in a_{GPL}/b_{GPL} and b_{GPL}/t_{GPL}. These effects, however, are seen to be much less pronounced when b_{GPL}/t_{GPL} is close to 10^3, beyond which the critical buckling temperature tends to be unchanged. For the same reason men-

tioned in Fig. 3, the critical buckling temperature of the U-GPLRC beam remains constant regardless of the variations in a_{GPL}/b_{GPL} and b_{GPL}/t_{GPL}.

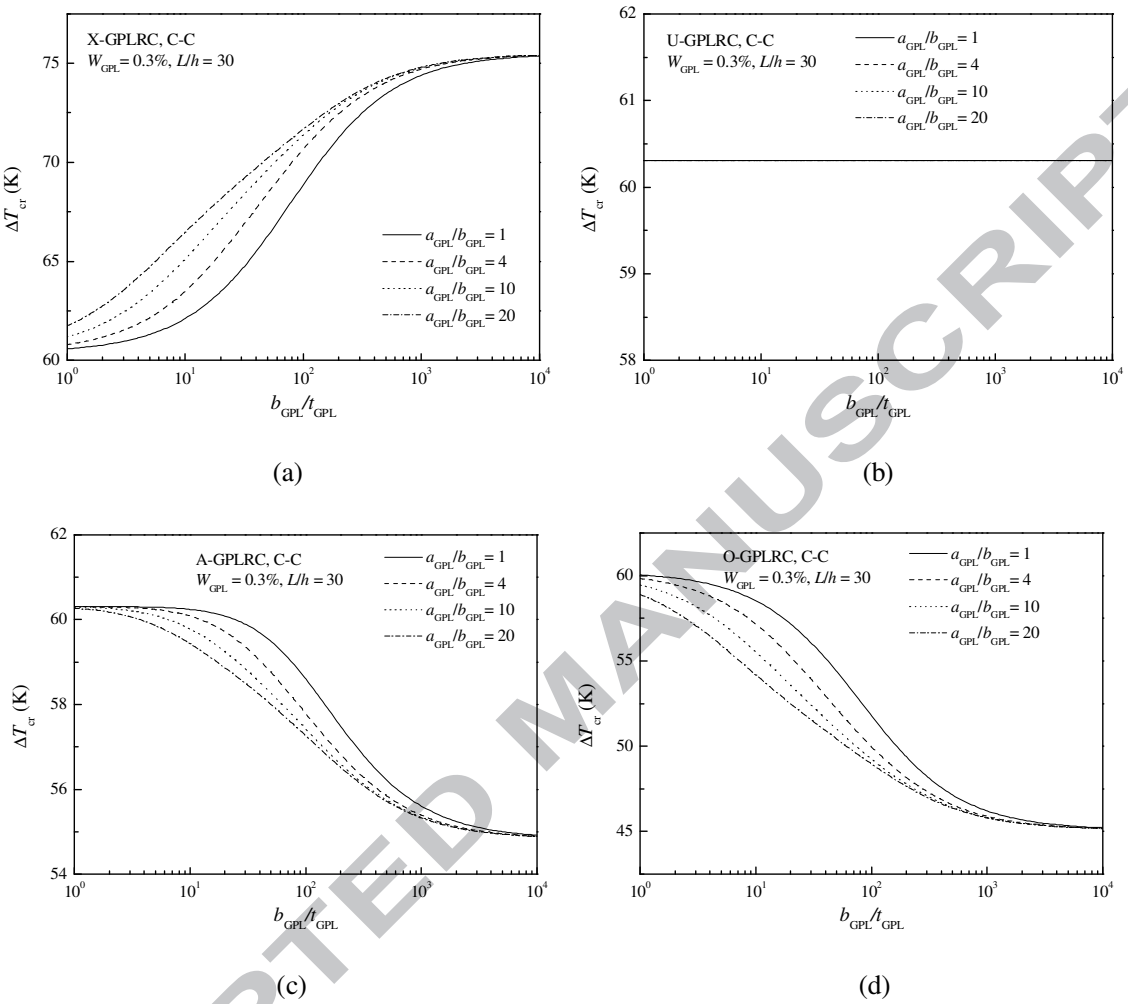

Fig. 5. Effects of GPL geometry and dimension on the critical buckling temperature rise of functionally graded multilayer GPLRC beams: (a) X-GPLRC, (b) U-GPLRC, (c) A-GPLRC, and (d) O-GPLRC.

Table 6 tabulates the critical buckling temperature rise for functionally graded multilayer X-GPLRC beams with different boundary conditions and slenderness ratios. As expected, the beam with rigid end supports (i.e. clamped ends) and smaller slenderness ratio has a considerably higher critical buckling temperature.

Table 6 Critical buckling temperature rise ΔT_{cr} (K) of functionally graded multilayer X-GPLRC beams with different boundary conditions and slenderness ratios (W_{GPL} = 0.3%)

BC	L/h = 25	L/h = 30	L/h = 35	L/h = 40
C-C	106.60	74.557	55.013	42.238
C-H	55.079	38.404	28.284	21.689
H-H	27.122	18.869	13.878	10.633

4.3 Thermo-mechanical vibration

The free vibration results of functionally graded multilayer GPLRC beams with L/h =10 subjected to thermo-mechanical loading are given in Table 7 and Figs. 6 and 7 where P_{cr} is the critical buckling load of the corresponding beam at $\Delta T = 0$ K.

Table 7 presents the first three dimensionless natural frequencies of C-C functionally graded multilayer GPLRC beams with different GPL distribution patterns subjected to a static axial compressive force. Note that $P_s/P_{cr} = 0$ corresponds to the case without a static axial force. Similarly to the observations in thermal buckling analysis, pattern X gives the highest natural frequencies, followed by patterns U, A, and O. Moreover, the natural frequencies are reduced as the compressive force is increased. This is because a compressive force creates a compressive initial stress state in the beam consequently, weakens the beam stiffness. It is also worthy of noting that the reinforcing effect of GPL nanofillers is not affected by the change of the initial axial compression. In other words, the percentage frequency increase of the beam due to the addition of GPLs remains the same regardless of the increase in P_s/P_{cr}.

Table 7 The first three dimensionless natural frequencies of C-C functionally graded multilayer GPLRC beams under a static axial compression (W_{GPL} = 0.3%, L/h = 10, ΔT = 0 K).

Multilayer beam	$P_s/P_{cr} = 0$			$P_s/P_{cr} = 0.25$			$P_s/P_{cr} = 0.50$		
	ω_1	ω_2	ω_3	ω_1	ω_2	ω_3	ω_1	ω_2	ω_3
Pure epoxy	0.5998	1.5248	2.7361	0.5228	1.4190	2.6144	0.4299	1.3036	2.4867
U-GPLRC	0.8475	2.1546	3.8662	0.7386	2.0051	3.6944	0.6075	1.8421	3.5139
X-GPLRC	0.9293	2.3325	4.1399	0.8103	2.1667	3.9464	0.6668	1.9856	3.7427
O-GPLRC	0.7508	1.9355	3.5171	0.6540	1.8045	3.3692	0.5375	1.6621	3.2142
A-GPLRC	0.8164	2.0835	3.7512	0.7114	1.9401	3.5876	0.5849	1.7840	3.4158

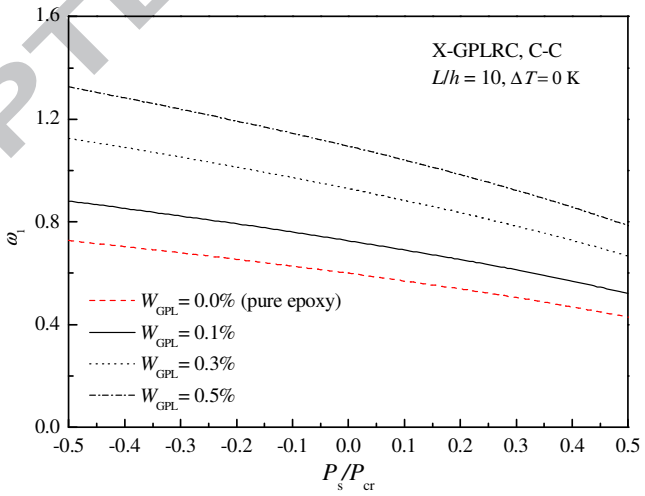

Fig. 6. Dimensionless fundamental frequency versus normalized static axial force for functionally graded multilayer X-GPLRC beams: effect of GPL weight fraction.

Fig. 6 compares the dimensionless fundamental frequency ω_1 versus normalized static axial force P_s/P_{cr} curves of functionally graded X-GPLRC beams with different GPL weight

fractions. The positive and negative values of P_s/P_{cr} represent the axial compressive and tensile forces, respectively. The fundamental frequency increases as the GPL weight fraction grows. In contrast to a compressive force, a tensile force strengthens the beam stiffness hence increases the fundamental frequency.

Fig. 7 displays the dimensionless fundamental frequency ω_1 versus normalized static axial force P_s/P_{cr} curves for functionally graded multilayer X-GPLRC beams subjected to initial thermo-mechanical loading. The results show that the fundamental frequency drops as the temperature increases and this effect becomes relatively more remarkable at a larger compressive force.

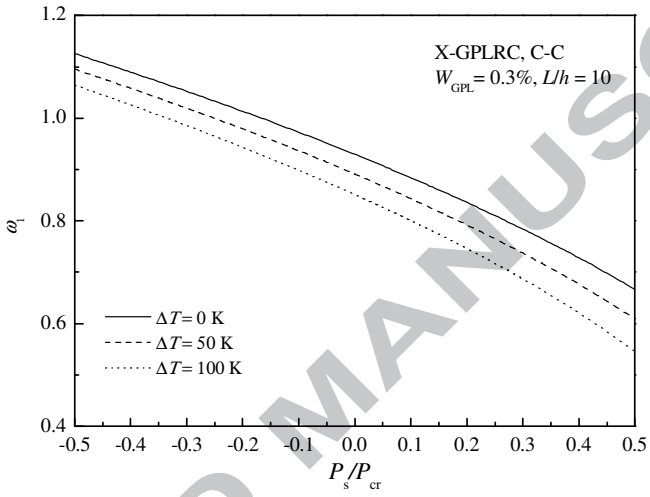

Fig. 7. Dimensionless fundamental frequency versus normalized static axial force for functionally graded multilayer X-GPLRC beams: effect of temperature change.

4.4 Dynamic instability

We next investigate the dynamic instability of functionally graded multilayer GPLRC beams under a periodic axial force. Unless otherwise stated, principle unstable regions, in terms of the dimensionless dynamic axial force P_d plotted against the dimensionless excitation frequency θ, are presented in Figs. 8-14 for C-C functionally graded multilayer X-GPLRC beams with W_{GPL} = 0.3%, L/h = 10, P_s/P_{cr} = 0.5, and ΔT = 0 K.

Figs. 8 and 9 plot the principal unstable regions for functionally graded multilayer GPLRC beams with different GPL distribution patterns and weight fractions, respectively. Among the four distribution patterns considered, pattern X gives the highest origin and narrowest unstable region. This is because in such a pattern, more GPLs are distributed near the top and bottom layers of the beam where the higher normal bending stress occurs, thus producing the best reinforcing effect. The results also show that the unstable region becomes wider at a lower GPL content. Compared with the pure epoxy beam, the origin of the unstable region of all GPLRC beams moves to the right as the GPL weight fraction increases. This is consistent with the observation in Table 7 where the fundamental frequency is found to be the lowest for the pure epoxy beam.

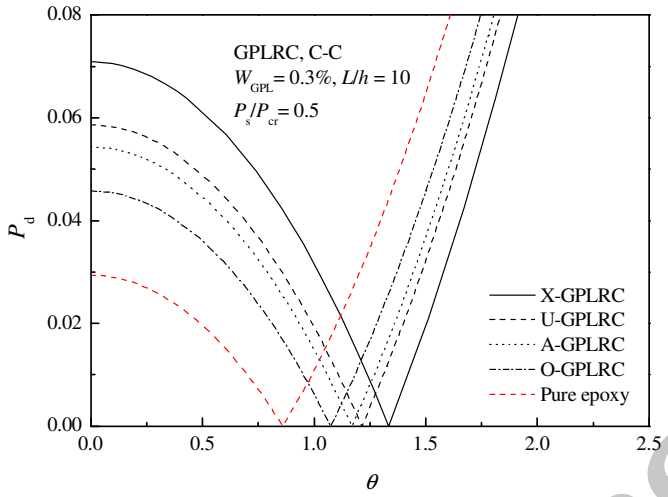

Fig. 8. Principal unstable regions of functionally graded multilayer GPLRC beams: effect of GPL distribution pattern.

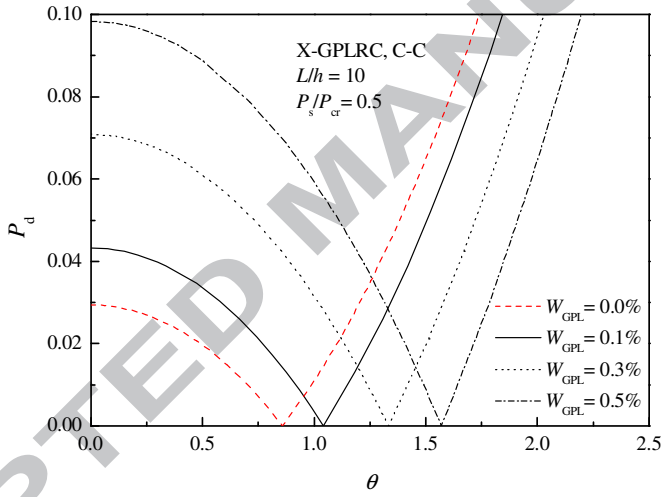

Fig. 9. Principal unstable regions of functionally graded multilayer X-GPLRC beams: effect of CNT weight fraction.

The effects of GPL geometry and dimension on the dynamic instability behaviour of functionally graded multilayer X-GPLRC beams are examined in Fig. 10(a) and (b) where the GPL width-to-thickness ratio and aspect ratio are fixed as $b_{GPL}/t_{GPL} = 10^3$ and $a_{GPL}/b_{GPL} = 4$, respectively. It is observed that the location and size of the unstable region are not sensitive to the GPL aspect ratio although the unstable region does move slightly to the right at a higher value of a_{GPL}/b_{GPL}. In contrast, an increase in GPL width-to-thickness ratio leads to a higher origin and a smaller unstable region. This effect is seen to be much less pronounced when b_{GPL}/t_{GPL} is larger than 10^3, which is very similar to the results in thermal buckling analysis.

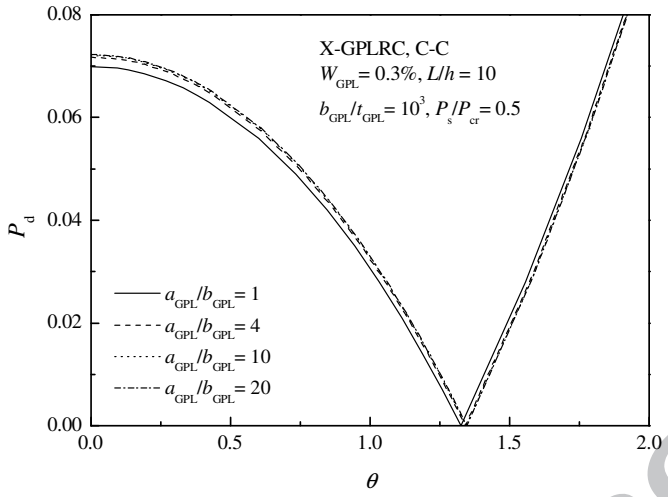

(a)

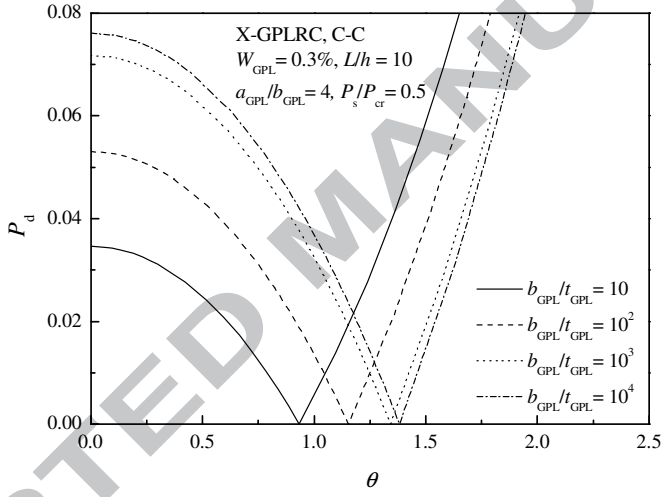

(b)

Fig. 10. Principal unstable regions of functionally graded multilayer X-GPLRC beams: effects of GPL (a) aspect ratio; and (b) width-to-thickness ratio.

Figs. 11 and 12 investigate the effects of static axial compressive force and temperature change on the dynamic instability of functionally graded multilayer X-GPLRC beams, respectively. The unstable region not only gets wider but also moves to the left as both the static axial compressive force and temperature increase. This is because, as mentioned before, both an axial compressive force and a temperature rise give rise to a compressive prestress in the beam and therefore weaken the beam stiffness. It is noteworthy that the effect of temperature change seems less noticeable than that of static axial compressive force due to the fact that the equivalent thermal force induced by the temperature rise in Fig. 12 is much smaller than the exerted static axial compressive force in Fig. 11.

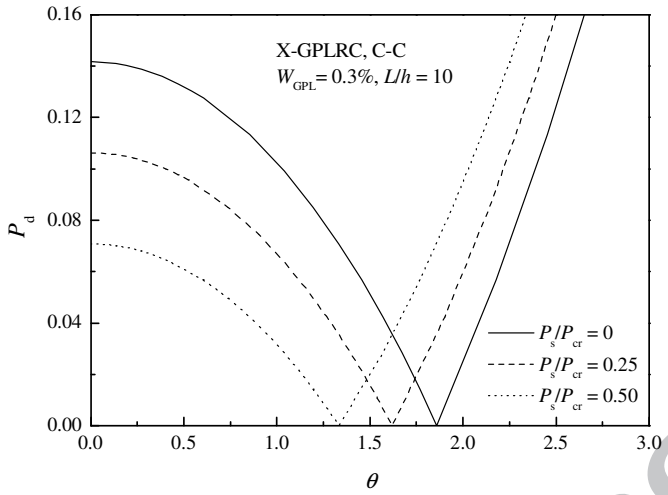

Fig. 11. Unstable regions of functionally graded multilayer X-GPLRC beams: effect of static compressive force.

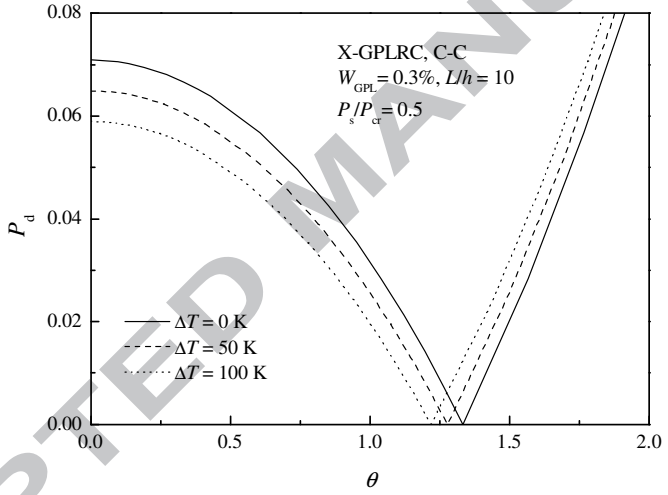

Fig. 12. Unstable regions of functionally graded multilayer X-GPLRC beams: effect of temperature change.

In order to illustrate the individual effect of slenderness ratio and boundary conditions, Figs. 13 and 14 present the principal unstable regions for functionally graded multilayer X-GPLRC beams with different slenderness ratios (L/h = 10, 20, 30) and boundary conditions (C-C, C-H, H-H), respectively. The C-C beam with a smaller slenderness ratio has a significantly higher origin and narrower unstable region because of its much greater bending rigidity.

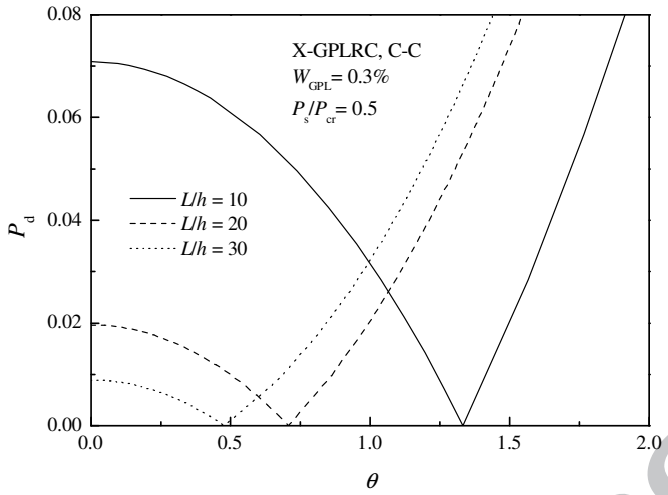

Fig. 13. Principal unstable regions of functionally graded multilayer X-GPLRC beams: effect of slenderness ratio.

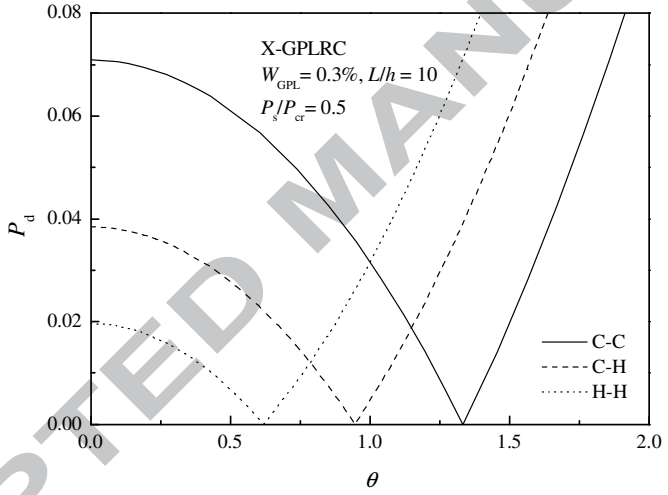

Fig. 14. Principal unstable regions of functionally graded multilayer X-GPLRC beams: effect of boundary conditions.

5. Concluding remarks

The dynamic instability of functionally graded multilayer graphene nanocomposite beams in thermal environment is investigated based on the FSDT. The differential quadrature method in conjunction with Bolotin's method is employed to obtain the principal unstable region for functionally graded multilayer GPLRC beams. The effective Young's modulus of GPLRCs is estimated by Halpin-Tsai micromechanics model. Comprehensive numerical results are presented in both tabular and graphical forms to examine the effects of the distribution pattern, geometry and dimension of GPL nanofillers, initial static axial load, as well as uniform temperature change on the dynamic instability behaviour. It is found that the GPL distribution pattern and weight fraction have important influences on the thermal buckling,

free vibration and dynamic instability of functionally graded multilayer GPLRC beams. The effects of GPL geometry and dimension tend to be much less significant when the GPL width-to-thickness ratio is greater than 10^3. Adding more GPLs and distributing them in pattern X can effectively increase the natural frequency and reduce the principal unstable region. An increase in either static axial compressive force or temperature or in both remarkably weakens the beam stiffness consequently leads to a lower fundamental frequency and a larger principal unstable region. The influences of slenderness ratio and boundary conditions are also discussed and demonstrated through illustrative numerical examples.

Acknowledgement

The work described in this paper was fully funded by the research grant from the Australian Research Council under Discovery Project scheme (DP160101978). The authors are grateful for this financial support.

References

[1] Winey KI, Vaia RA. Polymer nanocomposites. MRS Bull 2007;32(04):314-322.
[2] Fu S-Y, Feng X-Q, Lauke B, Mai Y-W. Effects of particle size, particle/matrix interface adhesion and particle loading on mechanical properties of particulate–polymer composites. Compos Part B-Eng 2008;39(6):933-961.
[3] Terrones M, Terrones H. The carbon nanocosmos: novel materials for the twenty-first century. Philos Trans R Soc London Ser A 2003;361(1813):2789-2806.
[4] Ji X-Y, Cao Y-P, Feng X-Q. Micromechanics prediction of the effective elastic moduli of graphene sheet-reinforced polymer nanocomposites. Model Simul Mater Sc 2010;18(4):045005.
[5] Iijima S. Helical microtubules of graphitic carbon. Nature 1991;354(6348):56-58.
[6] Iijima S, Ichihashi T. Single-shell carbon nanotubes of 1-nm diameter. Nature 1993;363:603-605.
[7] Lau K-T, Gu C, Gao G-H, Ling H-Y, Reid SR. Stretching process of single-and multi-walled carbon nanotubes for nanocomposite applications. Carbon 2004;42(2):426-428.
[8] Esawi AM, Farag MM. Carbon nanotube reinforced composites: potential and current challenges. Mater Design 2007;28(9):2394-2401.
[9] Thostenson ET, Ren Z, Chou T-W. Advances in the science and technology of carbon nanotubes and their composites: a review. Compos Sci Technol 2001;61(13):1899-1912.
[10] Shen H-S. Nonlinear bending of functionally graded carbon nanotube-reinforced composite plates in thermal environments. Compos Struct 2009;91(1):9-19.
[11] Liew KM, Lei ZX, Zhang LW. Mechanical analysis of functionally graded carbon nanotube reinforced composites: A review. Compos Struct 2015;120(0):90-97.
[12] Wu HL, Yang J, Kitipornchai S. Nonlinear vibration of functionally graded carbon nanotube-reinforced composite beams with geometric imperfections. Compos Part B-Eng 2016;90:86-96.
[13] Wu HL, Yang J, Kitipornchai S. Imperfection sensitivity of postbuckling behaviour of functionally graded carbon nanotube-reinforced composite beams. Thin Wall Struct 2016;108:225-233.

[14] Wu H, Kitipornchai S, Yang J. Imperfection sensitivity of thermal post-buckling behaviour of functionally graded carbon nanotube-reinforced composite beams. Appl Math Model 2016 (in press); DOI: 10.1016/j.apm.2016.10.045.
[15] Ke LL, Yang J, Kitipornchai S. Dynamic stability of functionally graded carbon nanotube-reinforced composite beams. Mech Adv Mater Struc 2013;20(1):28-37.
[16] Yang J, Ke L-L, Feng C. Dynamic buckling of thermo-electro-mechanically loaded FG-CNTRC beams. Int J Struct Stab Dy 2015;15(8):1540017.
[17] Lei Z, Zhang L, Liew K, Yu J. Dynamic stability analysis of carbon nanotube-reinforced functionally graded cylindrical panels using the element-free kp-Ritz method. Compos Struct 2014;113:328-338.
[18] Verdejo R, Bernal MM, Romasanta LJ, Lopez-Manchado MA. Graphene filled polymer nanocomposites. J Mater Chem 2011;21(10):3301-3310.
[19] Novoselov KS, Geim AK, Morozov SV, Jiang D, Zhang Y, Dubonos SV, Grigorieva IV, Firsov AA. Electric field effect in atomically thin carbon films. Science 2004;306(5696):666-669.
[20] Lee C, Wei X, Kysar JW, Hone J. Measurement of the elastic properties and intrinsic strength of monolayer graphene. Science 2008;321(5887):385-388.
[21] Balandin AA, Ghosh S, Bao W, Calizo I, Teweldebrhan D, Miao F, Lau CN. Superior thermal conductivity of single-layer graphene. Nano Lett 2008;8(3):902-907.
[22] Du X, Skachko I, Barker A, Andrei EY. Approaching ballistic transport in suspended graphene. Nat Nanotechnol 2008;3(8):491-495.
[23] Bonaccorso F, Colombo L, Yu G, Stoller M, Tozzini V, Ferrari AC, Ruoff RS, Pellegrini V. Graphene, related two-dimensional crystals, and hybrid systems for energy conversion and storage. Science 2015;347(6217):1246501.
[24] Tiwari A, Syväjärvi M. Graphene materials: fundamentals and emerging applications: John Wiley & Sons, 2015.
[25] Rafiee MA, Rafiee J, Wang Z, Song H, Yu Z-Z, Koratkar N. Enhanced mechanical properties of nanocomposites at low graphene content. ACS Nano 2009;3(12):3884-3890.
[26] Wang S, Tambraparni M, Qiu J, Tipton J, Dean D. Thermal expansion of graphene composites. Macromolecules 2009;42(14):5251-5255.
[27] Zhao X, Zhang Q, Chen D, Lu P. Enhanced mechanical properties of graphene-based poly (vinyl alcohol) composites. Macromolecules 2010;43(5):2357-2363.
[28] Liu J, Yan H, Jiang K. Mechanical properties of graphene platelet-reinforced alumina ceramic composites. Ceram Int 2013;39(6):6215-6221.
[29] Rahman R, Haque A. Molecular modeling of crosslinked graphene–epoxy nanocomposites for characterization of elastic constants and interfacial properties. Compos Part B-Eng 2013;54:353-364.
[30] Liu P, Jin Z, Katsukis G, Drahushuk LW, Shimizu S, Shih C-J, Wetzel ED, Taggart-Scarff JK, Qing B, Van Vliet KJ. Layered and scrolled nanocomposites with aligned semi-infinite graphene inclusions at the platelet limit. Science 2016;353(6297):364-367.
[31] Rafiee M, Rafiee J, Yu Z-Z, Koratkar N. Buckling resistant graphene nanocomposites. Appl Phys Lett 2009;95(22):223103.
[32] Song M, Kitipornchai S, Yang J. Free and forced vibrations of functionally graded polymer composite plates reinforced with graphene nanoplatelets. Compos Struct 2017;159:579-588.
[33] Halpin J, Kardos J. The Halpin-Tsai equations: a review. Polym Eng Sci 1976;16(5):344-352.
[34] Derek H. An Introduction to Composite Materials: Cambridge University Press, 1981.

[35] Harris B. Engineering Composite Materials: Institute of metals London, 1986.
[36] Shu C. Differential Quadrature and Its Application in Engineering. London: Springer, 2000.
[37] Wu H, Kitipornchai S, Yang J. Thermo-electro-mechanical postbuckling of piezoelectric FG-CNTRC beams with geometric imperfections. Smart Mater Struct 2016;25(9):095022.
[38] Wu H, Kitipornchai S, Yang J. Free vibration and buckling analysis of sandwich beams with functionally graded carbon nanotube-reinforced composite face sheets. Int J Struct Stab Dy 2015;15(7):1540011.
[39] Bert CW, Wang X, Striz AG. Differential quadrature for static and free vibration analyses of anisotropic plates. Int J Solids Struct 1993;30(13):1737-1744.
[40] Yang J, Kitipornchai S, Liew K. Non-linear analysis of the thermo-electro-mechanical behaviour of shear deformable FGM plates with piezoelectric actuators. Int J Numer Method Eng 2004;59(12):1605-1632.
[41] Bolotin VV. The Dynamic Stability of Elastic Systems. San Francisco, CA: Holden-Day, 1964.
[42] Yasmin A, Daniel IM. Mechanical and thermal properties of graphite platelet/epoxy composites. Polymer 2004;45(24):8211-8219.
[43] Liu F, Ming P, Li J. Ab initio calculation of ideal strength and phonon instability of graphene under tension. Phys Rev B 2007;76(6):064120.
[44] Available from: http://www.strem.com/catalog/v/06-0215/12/items_1034343-98-0. (Accessed: 28-Aug-2016)
[45] Khdeir A. Thermal buckling of cross-ply laminated composite beams. Acta Mech 2001;149(1-4):201-213.
[46] Ke LL, Yang J, Kitipornchai S, Xiang Y. Flexural vibration and elastic buckling of a cracked timoshenko beam made of functionally graded materials. Mech Adv Mater Struc 2009;16(6):488-502.
[47] Yan T, Kitipornchai S, Yang J. Parametric instability of functionally graded beams with an open edge crack under axial pulsating excitation. Compos Struct 2011;93(7):1801-1808.
[48] Reddy JN. Mechanics of laminated composite plates and shells: theory and analysis: CRC press, 2004.
[49] Yang J, Wu H, Kitipornchai S. Buckling and postbuckling of functionally graded multilayer graphene platelet-reinforced composite beams. Compos Struct 2017;161:111-118.